Image Quality of Virtual Monochromatic Reconstructions of Noncontrast CT on a Dual-Source CT Scanner in Adult Patients

Fasco van Ommen, Frans Kauw, Edwin Bennink, Jeremy J. Heit, Dylan N. Wolman, Jan Willem Dankbaar, Hugo W.A.M. de Jong, Max Wintermark

Rationale and Objectives: To evaluate the image quality of virtual monochromatic images (VMI) reconstructed from dual-energy dual-source noncontrast head CT with different reconstruction kernels.

Materials and Methods: Twenty-five consecutive adult patients underwent noncontrast dual-energy CT. VMI were retrospectively reconstructed at 5-keV increments from 40 to 140 keV using quantitative and head kernels. CT-number, noise levels (SD), signal-to-noise ratio (SNR), and contrast-to-noise ratio (CNR) in the gray and white matter and artifacts using the posterior fossa artifact index (PFAI) were evaluated.

Results: CT-number increased with decreasing VMI energy levels, and SD was lowest at 85 keV. SNR was maximized at 80 keV and 85 keV for the head and quantitative kernels, respectively. CNR was maximum at 40 keV; PFAI was lowest at 90 (head kernel) and 100 (quantitative kernel) keV. Optimal VMI image quality was significantly better than conventional CT.

Conclusion: Optimal image quality of VMI energies can improve brain parenchymal image quality compared to conventional CT but are reconstruction kernel dependent and depend on indication for performing noncontrast CT.

Keywords: Dual-energy CT; Virtual monochromatic images; Dual-source CT; Image quality.

Abbreviations: DECT dual-energy CT, **VMI** virtual monochromatic images, **NCCT** non-contrast CT, **ROI** region of interest, **HU** Hounsfield Unit, **SD** standard deviation, **SNR** signal-to-noise ratio, **CNR** contrast-to-noise ratio, **PFAI** posterior fossa artefact index, **Q1** first quantile, **Q3** third quantile

INTRODUCTION

Dual-energy CT (DECT) is an established method to improve image contrast, reduce imaging artifacts, and perform multimaterial decomposition (1–3). DECT is based on the simultaneous acquisition of two CT datasets at different energies (i.e., at a low and high energy) from the same CT scanner. Collection of high- and low-energy datasets allows energy-specific and therefore material-specific spectral attenuation curves to be obtained for any given CT voxel. The physical principle underlying DECT is the energy-dependence of materials; that is, the attenuation of a material changes with the incidence energy. The DECT dataset can then be used to generate different images, such as virtual noncontrast CT images (4–6), iodine maps (7,8), or virtual monochromatic images (VMI) (9,10). Virtual monochromatic images (11–14) have the potential to increase the conspicuity of cerebral pathology on noncontrast head CT (15–19), by its ability to reduce streak artifacts and beam-hardening artifacts, or to improve contrast attenuation in comparison to conventional CT imaging. However, VMI techniques and reconstruction algorithms vary among manufacturers. This means that optimal monochromatic energy

Acad Radiol 2021; 28:e323–e330

From the Department of Neuroradiology, Stanford University, Palo Alto, CA (F.v.O., F.K., J.J.H., D.N.W., M.W.); Department of Radiology and Nuclear Medicine, University Medical Center Utrecht, Mail E01.132, P.O. Box 85500, Utrecht 3508GA, the Netherlands (F.v.O., F.K., E.B., J.W.D., H.W.A.M.d.J.); Image Sciences Institute, University Medical Center Utrecht, Utrecht, the Netherlands (F.v.O., E.B., H.W.A.M.d.J.). Received April 14, 2020; revised May 13, 2020; accepted May 30, 2020. Funding information: This research has been made possible by the Dutch Heart Foundation and Technology Foundation STW, as part of their joint strategic research program (project number: 14732): ''Earlier recognition of cardiovascular diseases''. **Address Corresponding author:** F.V.O. e-mail: F.vanOmmen@umcutrecht.nl

https://doi.org/10.1016/j.acra.2020.05.038

levels cannot be translated from one manufacturer to the other (20). This means that for every manufacturer an extensive evaluation of image quality in VMI images is required. For the dual-source CT scanner, the image quality of monochromatic images has been well characterized in pediatric patients (21), but not in adults. In addition, the use of different reconstruction kernels on image quality in VMI has not been addressed in literature. To determine the quality of monochromatic reconstructions in adult patients, we present a quantitative analysis of the image quality of virtual monochromatic images reconstructed from noncontrast DECT images using a common quantitative kernel and a dedicated head kernel.

MATERIALS AND METHODS

Patients

We retrospectively identified 25 consecutive patients who underwent DECT on our institutional dual-source CT (Somatom Force, Siemens Healthineers, Germany). Inclusion criteria were at least 18 years old, presenting with clinical suspicion of stroke, and MRI was performed within 48 hours to evaluate presence of ischemia. These are patients in which we routinely acquire dual-energy CT data as part of our standard-of-care CT protocol. This study was approved by our institutional review board and complied with the Health Insurance Portability and Accountability Act. The need for informed consent was waived.

Imaging Protocol

Noncontrast dual-energy head CTs (NCCT) were acquired helically using tube voltages of 80 and 140 kVp with a tin filter, and tube currents of 640 and 320 mAs, respectively. The acquisition and reconstruction parameters are shown in Table 1. From the high- and low-energy reconstructions, VMI reconstructions were generated in 5-keV increments from 40 to 140 keV resulting in a total number of 21 VMI reconstructions. Each reconstruction was generated using both a quantitative (Q34s) and a head (J30s) reconstruction kernel (Syngo Via, Siemens Healthineers, Germany). The Q34s kernel is designed specifically for DECT imaging with beam-hardening correction for bone. Both kernels are so-called standard "medium smoothing" kernels, translating to a standard resolution and a moderate smoothing effect on the image, with subsequent improvements in contrast detail and reduced noise levels, but poorer edge definition relative to a harder kernel.

Quantitative Analysis

For every patient, one conventional NCCT series, which is a linear combination of both images from the two sources and 21 VMI reconstructions were obtained per kernel resulting in a total of 44 series of image volumes per patient. Similar to prior studies (15,21), a total of 12 regions of interest (ROI) of 25 mm^2 were drawn manually, and then adjusted to avoid partial volume averaging with adjacent tissue. If the patient had a visible infarct, the ROIs were drawn outside the infarcted area.

Paired ROIs were manually placed by an experienced radiology trainee (FK; 3 years of experience) bilaterally in the cortical gray matter of the frontal and parietotemporal lobes, the juxtacortical white matter, the deep thalamic gray matter, and the white matter of the posterior limb of the internal capsule. In addition, a 215 mm^2 ROI was placed in the interpretrous region of the posterior fossa on the slice with the greatest beam-hardening or streak artifact. For each ROI, the mean CT-number and noise level was recorded in Hounsfield Units (HU). The noise level (SD) was defined as the standard deviation of the HU values for each ROI. In addition, a measure for signal-to-noise ratio (SNR) was calculated for gray and white matter in every ROI:

$$SNR_{matter} = \frac{HU_{matter}}{SD_{matter}}.$$

To measure gray-white matter differentiation between adjacent gray and white matter ROI measurements, a gray-white matter contrast-to-noise ratio (CNR) was calculated as:

$$CNR = \frac{(HU_{GM} - HU_{WM})}{\sqrt{(SD_{GM}^2 + SD_{WM}^2)}}.$$

The posterior fossa artifact index (PFAI) was additionally calculated using a previously described method (22). The PFAI is defined as the standard deviation of the ROI in the posterior fossa, as a measure of HU variation, which thereby estimates the severity of beam-hardening or streak artifact.

Statistical Analysis

Patient characteristics were reported as median with first (Q1) and third (Q3) quantiles for continuous variables and frequencies with percentages for dichotomous variables. Measures of HU, SD, SNR, CNR, and PFAI were reported as mean ± standard deviation. We compared measures of HU, SD, SNR, CNR, and PFAI between VMI reconstructions by using repeated-measures of analysis of variance and a post-hoc Dunnett test. The maximum SNR, CNR, and minimum PFAI were compared to the conventional NCCT

TABLE 1. Dual-energy noncontrast CT acquisition and reconstruction parameters

Parameters	Scan type	Pitch	Beam collimation (mm)	Rotation time (s)	Slice thickness (mm)	Kernel	Matrix
	Helical	1.0	40 × 0.6 (24.0)	1.0	3.0	Q34s/J30s	512 × 512

measurements using paired t-tests. Differences between each reconstruction kernel for HU, SD, SNR, CNR and PFAI were analyzed with paired t-tests and the Bonferroni correction was applied to adjust for multiple testing. All analyses were conducted in SPSS (version 25.0, IBM, New York).

RESULTS

Baseline Patient Characteristics

Twenty-five patients (median age of 63 [Q1-Q3: 44-82] years, 36% female) with suspicion of stroke underwent noncontrast DECT. Fifteen patients were diagnosed with having a stroke on MRI (≤24 hours of onset), with a median presentation NIHSS of 2 (Q1-Q3: 0-8). There were 2 (8%) patients with known coronary artery disease, 5 (20%) with atrium fibrillation, 4 (16%) with diabetes, 14 (56%) with hypertension, 10 (40%) with hyperlipidemia, 2 (8%) with a prior cerebrovascular accident or intracranial hemorrhage, 5 (20%) were smokers and 13 (52%) were on antiplatelet or anticoagulant therapy.

Quantitative Analysis

In Figure 1, an example of a patient VMI reconstruction is shown, illustrating the differences in image quality, which will be evaluated.

CT Attenuation

The mean CT attenuation of the gray and white matter of each VMI reconstruction is plotted in Figure 2. There was a similar gradual decrease in the gray and white matter attenuation values with increasing reconstruction energy. Mean gray matter attenuation at 40 keV was 52.20 ± 12.25 HU and 72.94 ± 29.68 HU for the Q34s and J30s kernels, which decreased to 29.15 ± 2.95 HU and 27.36 ± 2.64 HU at 140 keV, respectively. There was a significant difference in attenuation between the J30s kernel compared to the Q34s kernel at all energy levels ($p < 0.001$) except 100 keV ($p > 0.875$). Mean white matter attenuation at 40 keV was 42.70 ± 7.86 HU and 46.53 ± 8.74 HU for the Q34s and J30s kernels, respectively, which decreased to 27.64 ± 2.89 HU and 27.30 ± 3.70 HU at 140 keV, respectively. There was a small but significant difference in white matter attenuation between the J30s and Q34s kernel at 40 to 90, 135 and 140 keV ($p < 0.002$).

CT Noise

From 40 to 85 keV, quantitative measures of noise in the gray and white matter decreased with increasing energy (Fig 3). Mean gray matter noise at 40 keV was 8.44 ± 2.03 HU and 9.25 ± 2.77 HU for Q34s and J30s kernels, respectively. Minimal noise was observed at 90 keV (3.41 ± 0.80 HU) using the Q34s kernel. The minimum noise at 90 keV was not significantly lower compared to 85 keV and 95 to 140keV ($p > 0.650$), whereas the other energies were significantly higher ($p < 0.001$). Minimal noise was observed at 85 keV (3.14 ± 0.67 HU) using the J30s kernel. Noise at 85 keV was significantly lower from all other monoenergetic reconstructions ($p < 0.001$), excepting the 80, 90 and 95 keV reconstructions ($p > 0.040$). There was a significant difference between the J30s and Q34s kernel for 40 and 65 to 100 keV ($p < 0.001$). Mean white matter noise measurements demonstrated a similar pattern, but with overall lower noise levels. Minimal noise was observed at 85 keV for both the Q34s and J30s kernels (3.08 ± 0.62 HU and 2.93 ± 0.61 HU, respectively). The noise at 85 keV was significantly lower than the noise at all other VMI energies ($p < 0.001$),

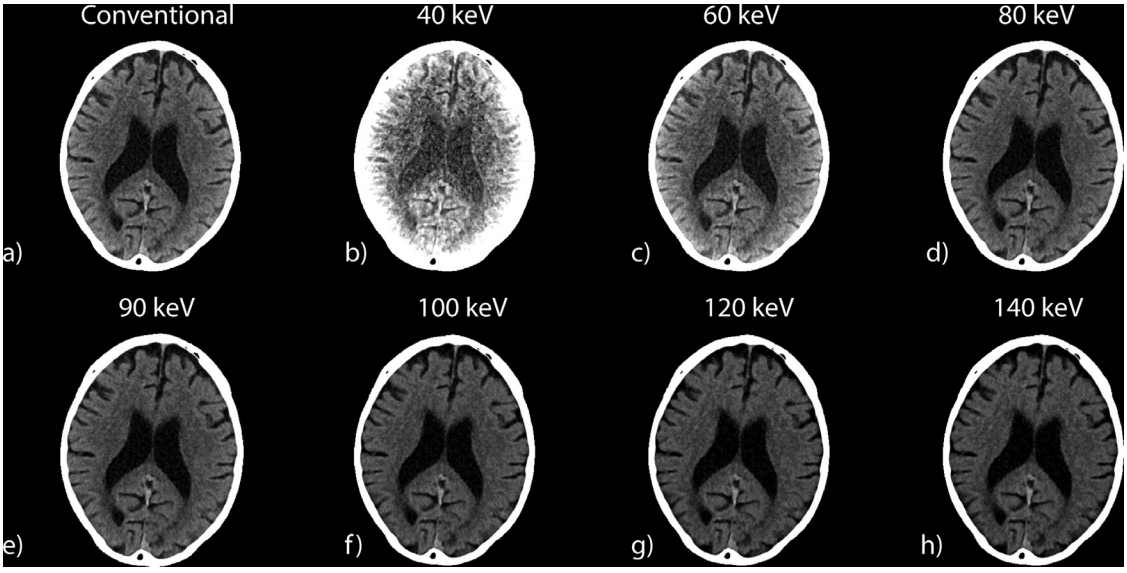

Figure 1. VMI and conventional NCCT reconstructed with the J30s kernel. Noise is more prone in the 40 keV (b), compared to the 140 keV (h) reconstructions. The window level/width is 40/80 for all reconstructions. The example shown here is exemplary for the Q34s kernel. NCCT, noncontrast computed tomography; VMI, virtual monochromatic images.

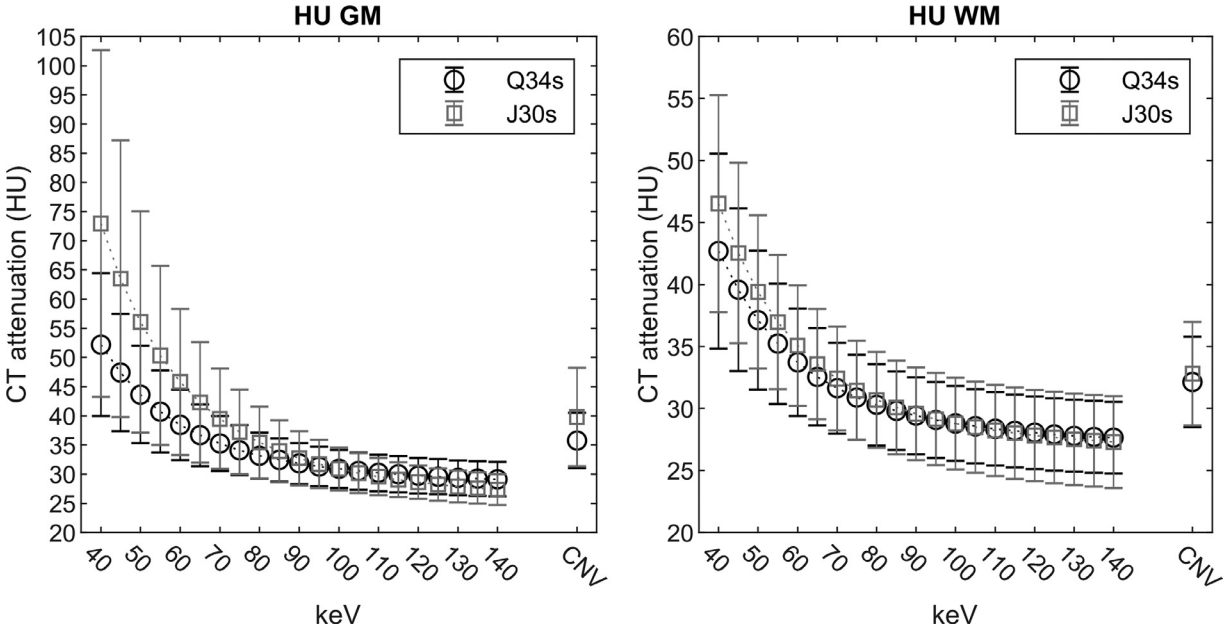

Figure 2. Mean ± standard deviation attenuation (HU) of the gray and white matter for the different virtual monochromatic images. The conventional NCCT (CNV) CT attenuation is shown for reference purposes. NCCT, noncontrast computed tomography.

except at 90 to 140 keV ($p = 1.000$) for the Q34s kernel. For the J30s kernel, the 85 keV reconstruction is significantly lower from all monoenergetic reconstructions ($p < 0.001$), except 80, 90−100 keV ($p > 0.002$). The noise for the J30s kernel is significant lower for 40 to 110 keV ($p < 0.001$) compared to the Q34s kernel.

Signal-to-Noise Ratio (SNR)

Gray matter SNR ranged from 6.56 ± 2.34 to 9.95 ± 2.41, and 8.16 ± 2.34 to 11.58 ± 3.35 with the Q34s and J30s kernels, respectively. An example of VMI using both kernels is shown in Figure 4.The maximum gray matter SNR was observed at 85 keV using the Q34s kernel (9.95 ± 2.41; Fig 5), which is significantly higher from all other monoenergetic reconstructions ($p < 0.001$), except for the 80 and 90 keV reconstructions ($p > 0.030$). For the J30s kernel, the maximum is at 80 keV (11.58 ± 3.35), which is significantly higher compared to 40 to 55 and 90 to 140 keV ($p < 0.001$). There is a significant increase in SNR between Q34s and J30s reconstruction kernels for the low energy levels (40−100 keV) ($p < 0.001$). White matter SNR ranged from 5.56 ± 1.48 to 10.00 ± 2.09 and 6.28 ± 1.75 to 10.69 ± 2.43 with a maximum at 85 (10.00 ± 2.09) and 80 keV (10.69 ± 2.43) for the Q34s and J30s kernel,

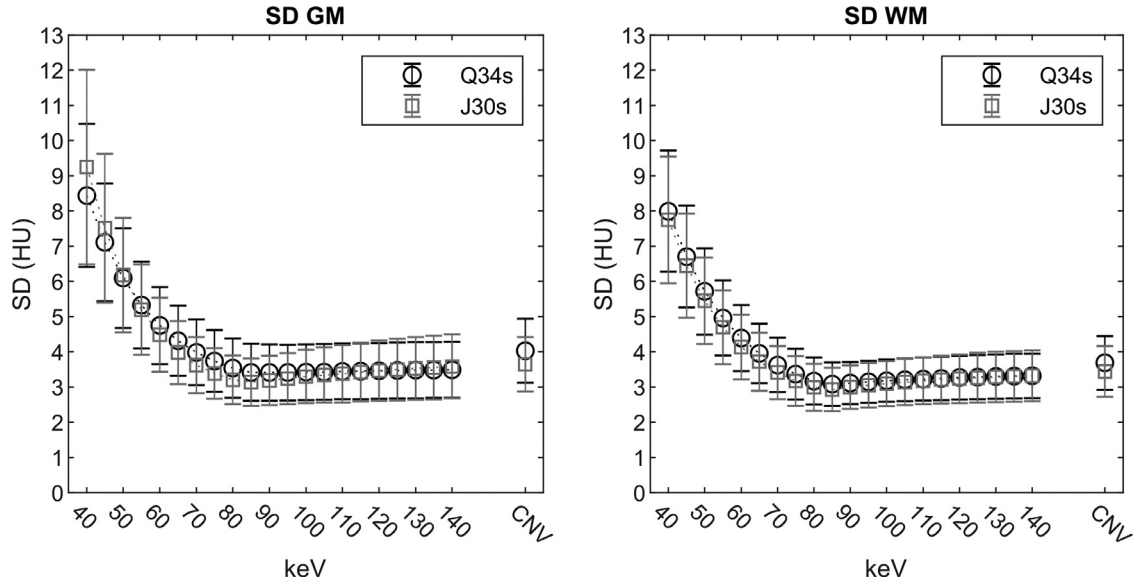

Figure 3. Mean ± standard deviation noise levels (SD) (HU) of the gray and white matter for virtual monochromatic images of 40 to 140 keV. The conventional NCCT (CNV) noise SD is shown for reference purposes. NCCT, noncontrast computed tomography

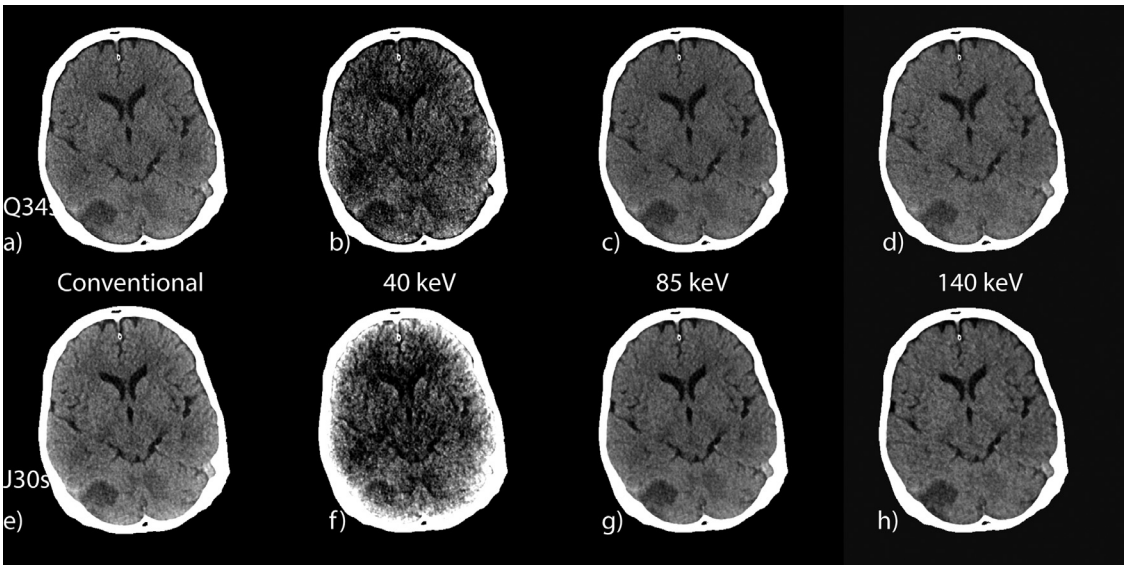

Figure 4. SNR is higher at 85 keV for both Q34s (c) and J30s kernel (g), compared to 40 keV (b and f) or 140 keV (d and h). The J30s increases the SNR compared to the Q34s kernel, even though the noise increases too. The window level/width is 40/80 for NCCT (a and e) and 85 keV (c and g), 35/80 for 140 keV (d and h) and 65/80 (Q34s) (b) and 70/80 (J30s) (f) for 40 keV to compensate for differences in mean CT attenuation. An infarction is visible in the right infratentorial brain. NCCT, noncontrast computed tomography; SNR, signal-to-noise ratio.

respectively. The maximum for the Q34s kernel is significantly higher for all VMI energy levels ($p < 0.001$), except for 80 keV ($p = 1.000$). For J30s, all but 85 and 90 keV ($p > 0.095$) are significantly lower than the maximum of 80 keV ($p < 0.001$). As compared to the Q34s kernel, there is a small but significant increase in SNR for the 40 to 105 keV monochromatic reconstructions using the J30s kernel ($p < 0.002$). The maximum SNR of the gray and white matter is significantly higher than that of the conventional NCCT ($p < 0.001$), except for the gray matter SNR of the J30s kernel ($p = 0.168$).

Contrast-to-Noise Ratio (CNR)

The mean CNR ranged from 0.81 ± 0.63 (140 keV) to 1.67 ± 0.72 (40 keV) and 0.71 ± 0.78 (140 keV) to 3.10 ± 1.45 (40 keV) for Q34s and J30s, respectively (Fig 6). The CNR was greatest at 40 keV (1.67 ± 0.72 (Q34s) and 3.10 ± 1.45 (J30s)), which was significantly greater than the CNR at 100 keV and higher energy levels ($p < 0.002$) for Q34s. The maximum was significantly greater than the CNR of 65 to 140 keV for J30s ($p < 0.001$). There was a significant increase in the CNR for the J30s kernel as compared to the Q34s kernel for reconstructions

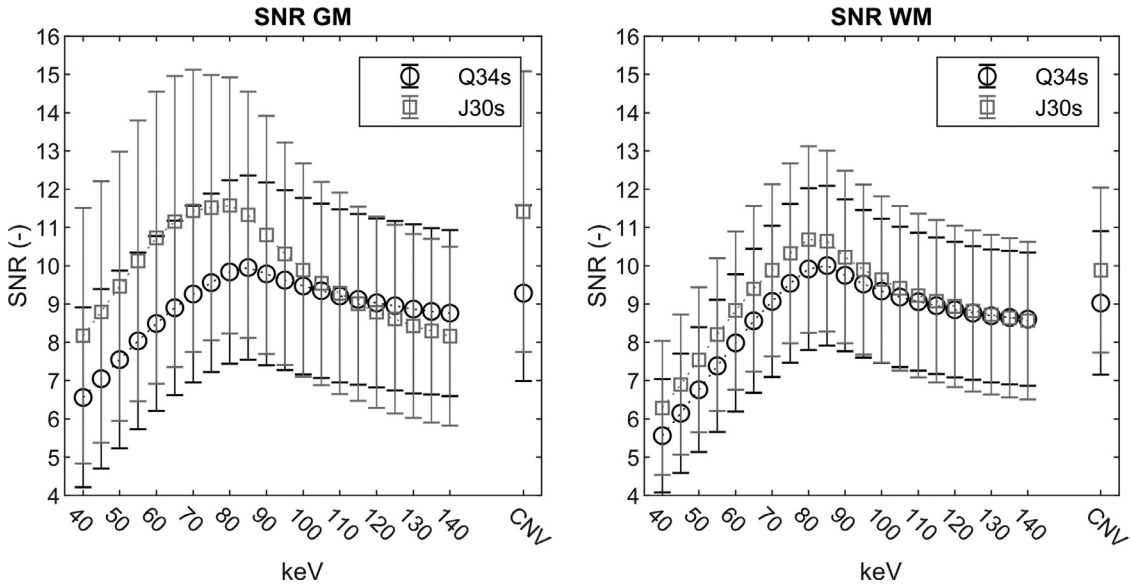

Figure 5. Mean ± standard deviation SNR of the gray and white matter for 40−140 keV monochromatic CT images. In addition, the SNR for the conventional NCCT (CNV) is shown as well. NCCT, noncontrast computed tomography.

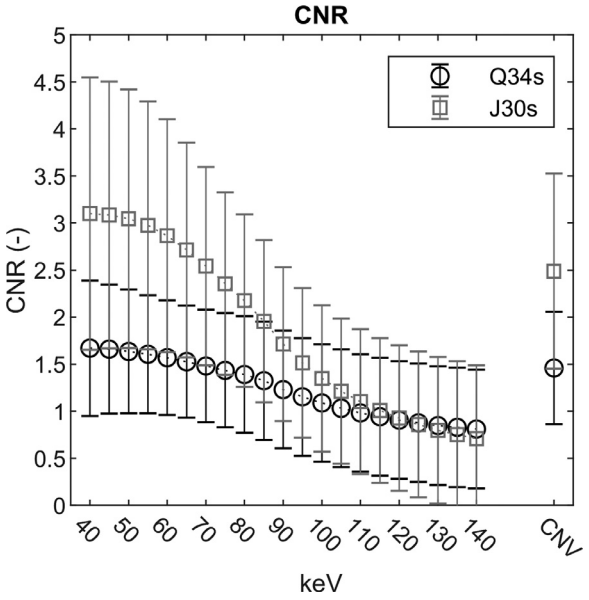

Figure 6. Mean ± standard deviation CNR of the different reconstruction kernels for monochromatic CT images. The CNR of the conventional NCCT (CNV) are shown as well, which is significantly lower than the maximum CNR of the VMI. CNR, contrast-to-noise ratio; NCCT, noncontrast computed tomography; VMI, virtual monochromatic images.

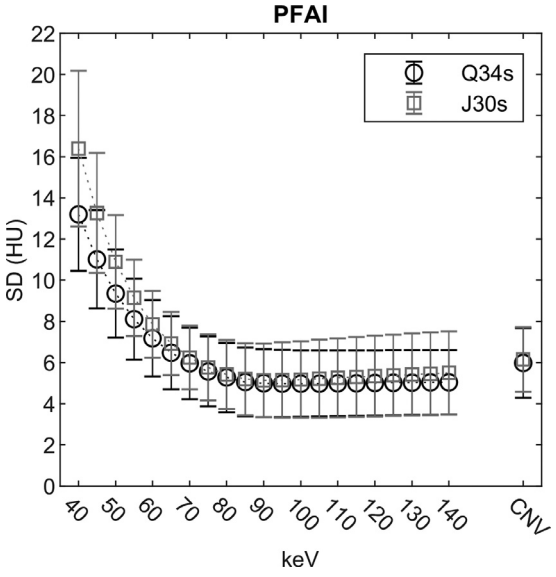

Figure 7. Mean ± standard deviation of the standard deviation of the attenuation (HU) of the posterior fossa for the different reconstruction kernels for the virtual monochromatic images and conventional NCCT reconstruction (CNV). NCCT, noncontrast computed tomography.

ranging from 40 to 110 keV ($p < 0.001$). The maximum CNR at 40 keV was significantly greater than the CNR of the conventional NCCT (1.46 ± 0.60 (Q34s) and 2.49 ± 1.04 (J30s)) for both kernels ($p < 0.001$).

Posterior Fossa Artifact Index

The PFAI ranged from 4.98 ± 1.63 HU to 13.20 ± 2.75 HU and 5.14 ± 1.79 HU to 16.39 ± 3.79 HU for the Q34s and J30s kernels, respectively (Fig 7). An example of the PFAI differences is shown in Figure 8. The minimum PFAI, or the smallest amount of artifacts, was observed at 90 keV (5.14 ± 1.79 HU) using the J30s kernel and 100 keV (4.98 ± 1.63 HU) using the Q34s, which was significantly lower than the PFAI at <80 keV ($p < 0.001$) for both kernels. The PFAI is lower for Q34s at all energies compared to J30s, the difference is significant for all energies ($p < 0.002$), except 55 to 105 keV ($p > 0.004$). The minimum PFAI is significantly

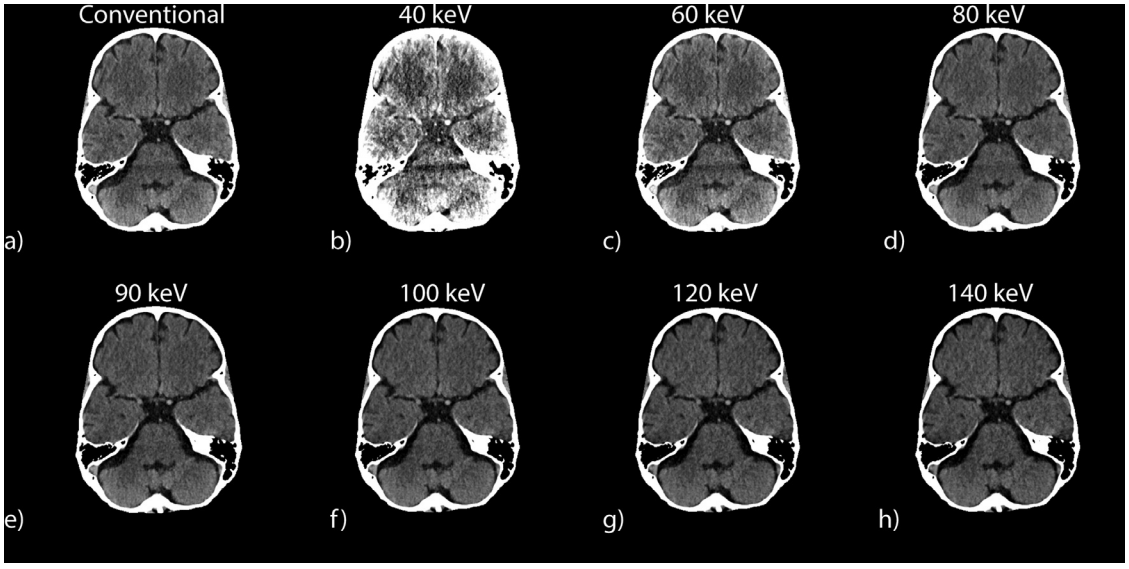

Figure 8. Example of change in noise in the posterior fossa, with different VMI and conventional images. The J30s reconstruction kernel is shown here. The window level/width is 40/80 for all images. The images shown here are exemplary for the Q34s kernel. VMI, virtual monochromatic images.

lower than the PFAI of the conventional NCCT (5.98 ± 1.69 HU (Q34s) and 6.15 ± 1.57 HU (J30s)) for both kernels ($p < 0.001$).

DISCUSSION

We found that depending on the used reconstruction kernel, DECT noise levels are reduced at 85 or 90 keV, and SNR was maximized at 80 and 85 keV. CNR was highest at 40 keV, but so was the PFAI. The PFAI was the smallest at 90 or 100 keV depending on the kernel.

To the best of our knowledge, this is the first study looking at virtual monochromatic images in adults using dual-source noncontrast DECT. In a previous study that evaluated the image quality of VMI in children (21), a similar trend for the CT attenuation of the gray and white matter was observed as compared to this study. Noise levels, however, were substantially lower compared to the previous study conducted in pediatric patients (21). The reduction in noise level was associated with a substantial increase in SNR in both the gray and white matter. The difference in noise levels can be explained by the acquisition settings; the peak voltage was similar, but the mAs were substantially higher in our study. This is likely because radiologists tend to accept images of lower quality in pediatric patients because of the focus on dose reduction, whereas, in adult patients with suspected stroke, image quality is paramount to detect subtle signs of early ischemia.

Interestingly, the CNR values we observed were comparable to the values observed in the pediatrics paper. In pediatric patients myelination may be incomplete depending on the age of the patients, and may be of variable attenuation due to different water-fat content ratios adding to the heterogeneity in their study, whereas in adults without underlying WM pathology, we have a relatively uniform WM attenuation. This may allow separate VMI reconstructions to be optimized for patient age, which is for a future study. The maximal CNR was observed at 40 keV in adults as opposed to 60 keV in pediatric patients. This shift is due to an increase in white matter attenuation at low keV. The maximum CNR is also not significantly larger than the CNR found up until 65 or 100 keV depending on the reconstruction kernel, suggesting comparable contrast in the images between the different VMI up until 65 or 100 keV.

The PFAI is highest in the low keV (40−60 keV) VMI, and is minimal at 90 (J30s) or 100 (Q34s) keV. Prior research (23) showed that higher VMI energies can be used to reduce beam hardening artifacts. This can be explained by the fact that generation of high keV monoenergetic images involves a higher contribution of the high kVp image, cancelling out beam hardening artifacts. The maximum SNR at 80 and 85 keV, and the minimum PFAI at 90 or 100 keV suggests that the indication for the head NCCT determines the required VMI energy. If a high SNR is required, a slightly lower keV is chosen, whereas if a reduction in artifacts is required a higher keV is needed.

The use of a head kernel resulted in a significant increase in SNR and CNR for the lower energies (40−100 keV) compared to the quantitative kernel. The GM-WM differentiation increased significantly using the head kernel. The kernel increased GM attenuation significantly, while maintaining a similar WM attenuation and noise levels as compared to the Q34s kernel. The maxima, however, shifted slightly to a different VMI energy. For the SNR, maximum shifted from 80 keV (Q34s) to 85 keV (J30s) and for PFAI from 100 (Q34s) to 90 keV (J30s). Because the maximum SNR, CNR and minimum PFAI are VMI energy dependent, but also reconstruction kernel dependent, the selection of a reconstruction kernel should be carefully considered and investigated. If the scan is used for small malformations close to the skull or in the infratentorial area a quantitative kernel at 100 keV would be preferred because the artifact index is minimized at this energy level. With more supratentorial diagnostics, for example, hemorrhage detection or identification of brain masses in which high SNR and CNR are more important a reconstruction with a head kernel at 65 keV would be preferred, which is a trade-off between maximum CNR and maximum SNR. In addition, the exaggeration of the gray-white matter distinction using the head kernel could be advantageous when assessing ischemic changes in the brain.

Our study has several limitations, including its retrospective design and relatively small number of patients. Also, we solely focused on assessing image quality parameters. Conclusions on diagnostic accuracy in a clinical setting cannot be drawn from the presented data. Lastly, in this study we choose to use CT-number to estimate the SNR, to be able to compare with prior research. Of course if a different metric or definition for signal is chosen (e.g. the linear attenuation coefficient), this may alter the SNR value. This would, however, not change the general conclusions of this study.

CONCLUSION

In conclusion, the use of virtual monochromatic images can improve brain parenchymal image quality compared to conventional NCCT. The desired energy level for the VMI reconstruction should be based on the indication for performing the NCCT. To minimize beam-hardening and streak artifacts an optimal energy of 90 or 100 keV should be chosen, whereas if one seeks to maximize SNR and CNR one should look at 65 or 80 keV depending on the used reconstruction kernel. This shows that the use of different reconstruction kernels can affect image quality significantly, and therefore must be selected carefully.

REFERENCES

1. Johnson TRC, Krauß B, Sedlmair M, et al. Material differentiation by dual energy CT: initial experience. Eur Radiol 2007; 17:1510–1517. doi:10.1007/s00330-006-0517-6.
2. Petersilka M, Bruder H, Krauss B, et al. Technical principles of dual source CT. Eur J Radiol 2008; 68:362–368. doi:10.1016/j.ejrad.2008.08.013.

3. McCollough CH, Leng S, Yu L, Fletcher JG. Dual- and multi-energy CT: principles, technical approaches, and clinical applications. Radiology 2015; 276:637–653. doi:10.1148/radiol.2015142631.
4. Gupta R, Phan CM, Leidecker C, et al. Evaluation of dual-energy CT for differentiating intracerebral hemorrhage from iodinated contrast material staining. Radiology 2010; 257:205–211. doi:10.1148/radiol.10091806.
5. Tijssen MPM, Hofman PAM, Stadler AAR, et al. The role of dual energy CT in differentiating between brain haemorrhage and contrast medium after mechanical revascularisation in acute ischaemic stroke. Eur Radiol 2014; 24:834–840. doi:10.1007/s00330-013-3073-x.
6. Ananthakrishnan L, Rajiah P, Ahn R, et al. Spectral detector CT-derived virtual non-contrast images: comparison of attenuation values with unenhanced CT. Abdom Radiol. 2017. doi:10.1007/s00261-016-1036-9.
7. Chandarana H, Megibow AJ, Cohen BA, et al. Iodine quantification with dual-energy CT: phantom study and preliminary experience with renal masses. Am J Roentgenol 2011; 196:693–700. doi:10.2214/AJR.10.5541.
8. Song KD, Kim CK, Park BK, et al. Utility of iodine overlay technique and virtual unenhanced images for the characterization of renal masses by dual-energy CT. Am J Roentgenol 2011; 197:1076–1082. doi:10.2214/AJR.11.6922.
9. Zhou C, Zhao YE, Luo S, et al. Monoenergetic imaging of dual-energy CT reduces artifacts from implanted metal orthopedic devices in patients with factures. Acad Radiol 2011; 18:1252–1257. doi:10.1016/j.acra.2011.05.009.
10. Wellenberg RHH, Boomsma MF, van Osch JAC, et al. Quantifying metal artefact reduction using virtual monochromatic dual-layer detector spectral CT imaging in unilateral and bilateral total hip prostheses. Eur J Radiol 2017; 88:61–70. doi:10.1016/j.ejrad.2017.01.002.
11. Dong Y, Shi AJ, Wu JL, et al. Metal artifact reduction using virtual monochromatic images for patients with pedicle screws implants on CT. Eur Spine J 2016; 25:1754–1763. doi:10.1007/s00586-015-4053-4.
12. Jung DC, Oh YT, Kim MD, et al. Usefulness of the virtual monochromatic image in dual-energy spectral CT for decreasing renal cyst pseudoenhancement: a phantom study. Am J Roentgenol 2012; 199:1316–1319. doi:10.2214/AJR.12.8660.
13. Yamada Y, Jinzaki M, Tanami Y, et al. Virtual monochromatic spectral imaging for the evaluation of hypovascular hepatic metastases. Invest Radiol 2012; 47:292–298. doi:10.1097/RLI.0b013e318240a874.
14. Pessis E, Campagna R, Sverzut J-M, et al. Virtual monochromatic spectral imaging with fast kilovoltage switching: reduction of metal artifacts at CT. RadioGraphics 2013; 33:573–583. doi:10.1148/rg.332125124.
15. Pomerantz SR, Kamalian S, Zhang D, et al. Virtual monochromatic reconstruction of dual-energy unenhanced head CT at 65−75 keV maximizes image quality compared with conventional polychromatic CT. Radiology 2013; 266:318–325. doi:10.1148/radiol.12111604.
16. Lam S, Gupta R, Levental M, et al. Optimal virtual monochromatic images for evaluation of normal tissues and head and neck cancer using dual-energy CT. Am J Neuroradiol 2015; 36:1518–1524. doi:10.3174/ajnr.A4314.
17. Hwang WD, Mossa-Basha M, Andre JB, et al. Qualitative comparison of noncontrast head dual-energy computed tomography using rapid voltage switching technique and conventional computed tomography. J Comput Assist Tomogr 2016; 40:320–325. doi:10.1097/RCT.0000000000000350.
18. Zhao X-M, Wang M, Wu R-Z, et al. Dual-layer spectral detector CT monoenergetic reconstruction improves image quality of non-contrast cerebral CT as compared with conventional single energy CT. Eur J Radiol 2018; 103:131–138. doi:10.1016/j.ejrad.2018.04.015.
19. Neuhaus V, Abdullayev N, Große Hokamp N, et al. Improvement of image quality in unenhanced dual-layer CT of the head using virtual monoenergetic images compared with polyenergetic single-energy CT. Invest Radiol 2017; 52:470–476. doi:10.1097/RLI.0000000000000367.
20. Potter CA, Sodickson AD. Dual-energy CT in emergency neuroimaging: added value and novel applications. RadioGraphics 2016; 36:2186–2198. doi:10.1148/rg.2016160069.
21. Park J, Choi YH, Cheon JE, et al. Advanced virtual monochromatic reconstruction of dual-energy unenhanced brain computed tomography in children: comparison of image quality against standard mono-energetic images and conventional polychromatic computed tomography. Pediatr Radiol 2017; 47:1648–1658. doi:10.1007/s00247-017-3908-8.
22. Rozeik C, Kotterer O, Preiss J, et al. Cranial CT artifacts and gantry angulation. J Comput Assist Tomogr 1991; 15:381–386.
23. Hixson HR, Leiva-Salinas C, Sumer S, et al. Utilizing dual energy CT to improve CT diagnosis of posterior fossa ischemia. J Neuroradiol 2016; 43:346–352. doi:10.1016/j.neurad.2016.04.001.